Multiple Dirac nodes and symmetry protected Dirac nodal line in orthorhombic α-RhSi

Shirin Mozaffari , Niraj Aryal, Rico Schönemann, Kuan-Wen Chen, Wenkai Zheng, Gregory T. McCandless, Julia Y. Chan, ³ Efstratios Manousakis, ^{1,2,4,†} and Luis Balicas ^{1,2,‡}

¹National High Magnetic Field Laboratory, Florida State University, Tallahassee, Florida 32310, USA ²Department of Physics, Florida State University, Tallahassee, Florida 32306, USA ³Department of Chemistry and Biochemistry, The University of Texas at Dallas, Richardson, Texas 75080, USA ⁴Department of Physics, University of Athens, Panepistimioupolis, Zografos, 157 84 Athens, Greece



(Received 6 February 2020; revised 26 August 2020; accepted 27 August 2020; published 15 September 2020)

Exotic multifold topological excitations have been predicted and were recently observed in transition metal silicides like β -RhSi. Herein, we report that interesting topological features of RhSi are also observed in its orthorhombic α phase, which displays multiple types of Dirac nodes very close to the Fermi level ε_F . We discuss the symmetry analysis, band connectivity along high-symmetry lines using group representations, band structure, the nature of the Dirac points and of a nodal line occurring near ε_F which is protected by the crystalline symmetry. The de Haas-van Alphen effect indicates a Fermi surface in agreement with the calculations. We find an elliptically shaped nodal line very close to ε_F around and near the S point on the $k_v - k_z$ plane that results from the intersection of two upside-down Dirac cones. Both Dirac points of the participating Kramers degenerate bands are only 5 meV apart; hence, an accessible magnetic field might induce a crossing between the spin-up partner of the upper Dirac cone and the spin-down partner of the lower Dirac cone, possibly explaining the anomalies observed in the magnetic torque. α -RhSi is a unique system since all bands crossing ε_F emerge from Dirac nodes.

DOI: 10.1103/PhysRevB.102.115131

I. INTRODUCTION

Gapless electronic excitations observed in condensedmatter systems are analogous to three types of fermioniclike elementary particles predicted by the standard model of particle physics, namely, Dirac, Weyl, and Majorana fermions [1–6]. Compounds hosting such excitations include Dirac and Weyl semimetals with degenerate nodal points near their ε_F . In addition to the two- and fourfold-degenerate Weyl and Dirac semimetals, other classes of semimetals with three-, six-, and eightfold degeneracy at high-symmetry points (HSPs) within their Brillouin zone (BZ) have been predicted [7-11].

For instance, exotic multifold topological excitations have been theoretically predicted [9,12] and were recently observed in a family comprising transition metals combined, for example, with elements of the carbon group (or tetrels) or in aluminides, including CoSi [10,13,14], β -RhSi [15], AlPt [16], and RhSn [17]. These compounds belong to the noncentrosymmetric space group (SG) P2₁3 (No. 198) for which the calculations predict Weyl nodes characterized by Chern numbers C > 1 at specific HSPs within their BZ, leading to several extended Fermi arcs on their surface. Angle-resolved photoemission spectroscopy has verified the presence of chiral spin-1 fermions at the Γ point and charge-2 fermions at the R point of the BZ with $C = \pm 2$ in CoSi and β -RhSi [13–15], although |C| = 4 was reported for PdGa [18]. Due to their nontrivial

Chern numbers, chiral topological compounds are predicted to display novel effects like magnetochiral anisotropy [19] and the quantized circular photogalvanic effect [20,21].

Dirac semimetals, which, in contrast to Weyl systems, preserve Kramers degeneracy, have also attracted a lot of attention. Compounds like Cd₃As₂ [22] unveiled a possible novel mechanism for topological protection against backscattering [23]. Evidence for the chiral anomaly among field-induced Weyl nodes was collected from Na₃Bi upon lifting time reversal symmetry (TRS) and hence Kramers degeneracy [24,25]. This splitting of the Dirac into Weyl nodes has led to the prediction [26] and subsequent observation [27] of new cyclotron orbits involving Fermi arcs on the surface of Cd₃As₂ with an associated quantum Hall effect [28]. Topological nodal line (NL) systems, i.e., compounds where two bands cross to form closed lines within the BZ [29–32], are another very active area of research. In general, spin-orbit coupling gaps the NLs unless they are protected by some crystalline symmetry in addition to inversion and TRS [29-31]. Prominent examples include the ZrSiS family that displays Dirac NLs at both symmorphic and nonsymmorphic positions [33] and the correlated Dirac NL iridate CaIrO₃ [34]. Among the aforementioned compounds, only N₃Bi [35] and those belonging to SG 198 are known to solely possess either linearly dispersing or topological nontrivial bands crossing ε_F . Most of the topological semimetals display coexistence with quadratic bands or trivial carriers.

Here, we have grown crystalline α -RhSi, which adopts the orthorhombic MnP (B31) structure type (centrosymmetric space group *Pnma*, No. 62), and we report, through group theory analysis and density functional theory (DFT) calculations,

^{*}These authors contributed equally to this work.

[†]stratos@physics.fsu.edu

^{*}balicas@magnet.fsu.edu

the existence of a symmetry protected NL, which is the result of the intersection of double Dirac cones, with their cones located relatively close to the Fermi energy. In addition, we report the existence of other Dirac nodes very close to ε_F . The DFT calculations are confirmed via measurements of the de Haas–van Alphen (dHvA) effect which unveils a Fermi surface (FS) whose topography is in reasonably good agreement with the predictions. For certain field orientations, the magnetic torque suggests transitions between distinct topological regimes, e.g., from Dirac to Weyl-like.

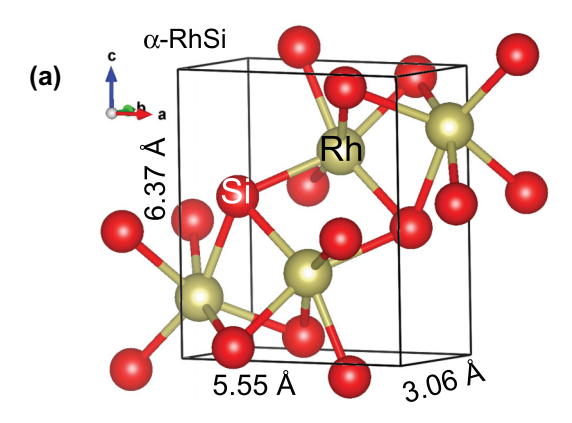
II. EXPERIMENTAL DETAILS

Single crystals of α -RhSi were obtained using a moltentellurium flux. Elemental Si, Rh, and Te powder with a molar ratio of 1:1:20 were loaded in an alumina crucible and then sealed in a fused silica ampule under vacuum. The tube was then heated to $1050\,^{\circ}\text{C}$, held there for 24 h, and then cooled at a rate of $2\,^{\circ}\text{C/h}$ to $700\,^{\circ}\text{C}$. At this temperature the flux was separated from the crystals by inverting the tube and centrifuging. The as-obtained crystals had dimensions ranging from 200 to $700\,\mu\text{m}$.

Single-crystal x-ray diffraction was used to orient the crystal and obtain the lattice parameters. The orientation was performed using a Bruker D8 Quest Kappa single-crystal xray diffractometer equipped with an I μ S microfocus source (Mo $K\alpha$, $\lambda = 0.71073$ Å). X-ray diffraction confirmed that the crystal structure adopts the space group Pnma with lattice parameters of a = 5.5518(9) Å, b = 3.0637(6) Å, and c =6.3738(11) Å. In the Supplemental Material (SM) [36] we provide additional information concerning the x-ray diffraction analysis (Table I and Fig. S1), as well as the anomalous behavior of the magnetic torque (Fig. S2) discussed below, the angular dependence of the dHvA frequencies and the extraction of the carrier effective masses (Fig. S3), and details concerning the DFT and the generalized gradient approximation plus electronic correlation (GGA + U) calculations [37–42] in Figs. S4 and S5.

Conventional magnetotransport experiments were performed in a physical property measurement system (Quantum Design) under magnetic fields up to $\mu_0H=9$ T and temperatures as low as 2 K using a conventional four-terminal method. Magnetization measurements under fields up to $\mu_0H=7$ T were performed in a commercial superconducting quantum interference device magnetometer (Quantum Design). The angular dependence of the dHvA effect under continuous fields up to $\mu_0H=31$ T was performed in a resistive Bitter magnet at the National High Magnetic Field Laboratory in Tallahassee, Florida, using a piezoresistive microcantilever technique. A 3 He cryostat where the samples were immersed in liquid 3 He, in combination with a rotating probe, was used for high-field experiments at temperatures down to 0.35 K.

Figure 1(a) displays the crystallographic structure of α -RhSi along with its unit cell and lattice constants. Figure S1 in the SM shows the single-crystal x-ray diffraction patterns along different hkl planes, revealing high crystallinity. Figure 1(b) displays the magnetic torque $\tau = (\mu_0 H)\Delta M \sin 2\theta/2$, where ΔM is the anisotropy in the magnetization $M_{c,ab} = \chi_{c,ab}(\mu_0 H)$ (χ_i is the susceptibility along the i axis) for a layered system as a function of magnetic



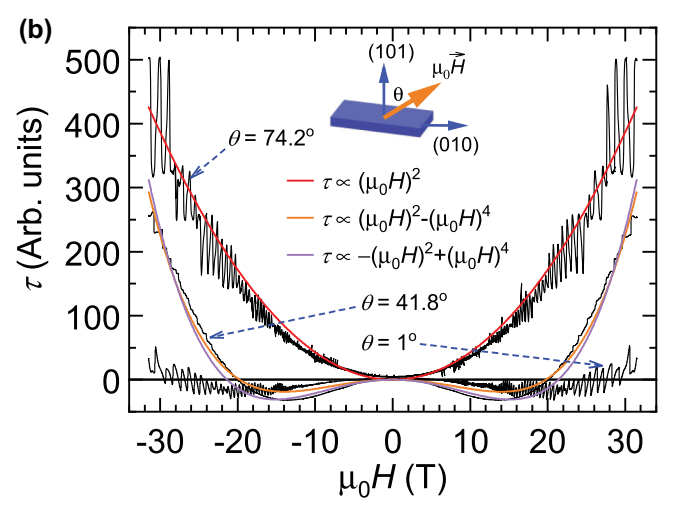


FIG. 1. (a) Crystal structure of α -RhSi. (b) Magnetic torque τ as a function of the magnetic field $\mu_0 H$ for several angles θ at T=350 mK. θ is the angle between $\mu_0 H$ and the (101) direction of the crystal. Red, orange, and purple lines indicate different polynomial fittings.

field $\mu_0 H$ and for three different angles θ between $\mu_0 H$ and the (101) direction. τ is expected to behave as $\propto (\mu_0 H)^2$, as illustrated by the fit (red line) to the $\tau(\mu_0 H)$ trace collected at $\theta = 74.2^{\circ}$. The superimposed oscillatory component corresponds to the dHvA effect. In contrast, at low angles the background of $\tau(\mu_0 H)$ can be fitted only to combinations of quadratic and quartic terms. This sharp change in the behavior of $\tau(\mu_0 H)$ cannot be reconciled with the diamagnetic response of α -RhSi. In Fig. S2 we plot the angular dependence of both the quadratic and quartic terms. The quadratic term changes its sign as a function of θ following the $\sin 2\theta$ dependence. The quartic term emerges beyond $\theta \sim 30^{\circ}$, indicating that it is orientation dependent or that it reflects the anisotropy of the Zeeman effect, pointing to the possibility of a topological phase transition. Further below we provide the electronic band structure (EBS) calculations revealing a double Dirac structure whose nodes are very close in energy and hence susceptible to the external field.

III. MAGNETOTRANSPORT MEASUREMENTS

Figure 2 displays the characterization of our α -RhSi crystals, e.g., the resistivity as a function of the temperature T, indicating a small residual resistivity $\rho_0 \sim 0.78~\mu\Omega$ cm. In

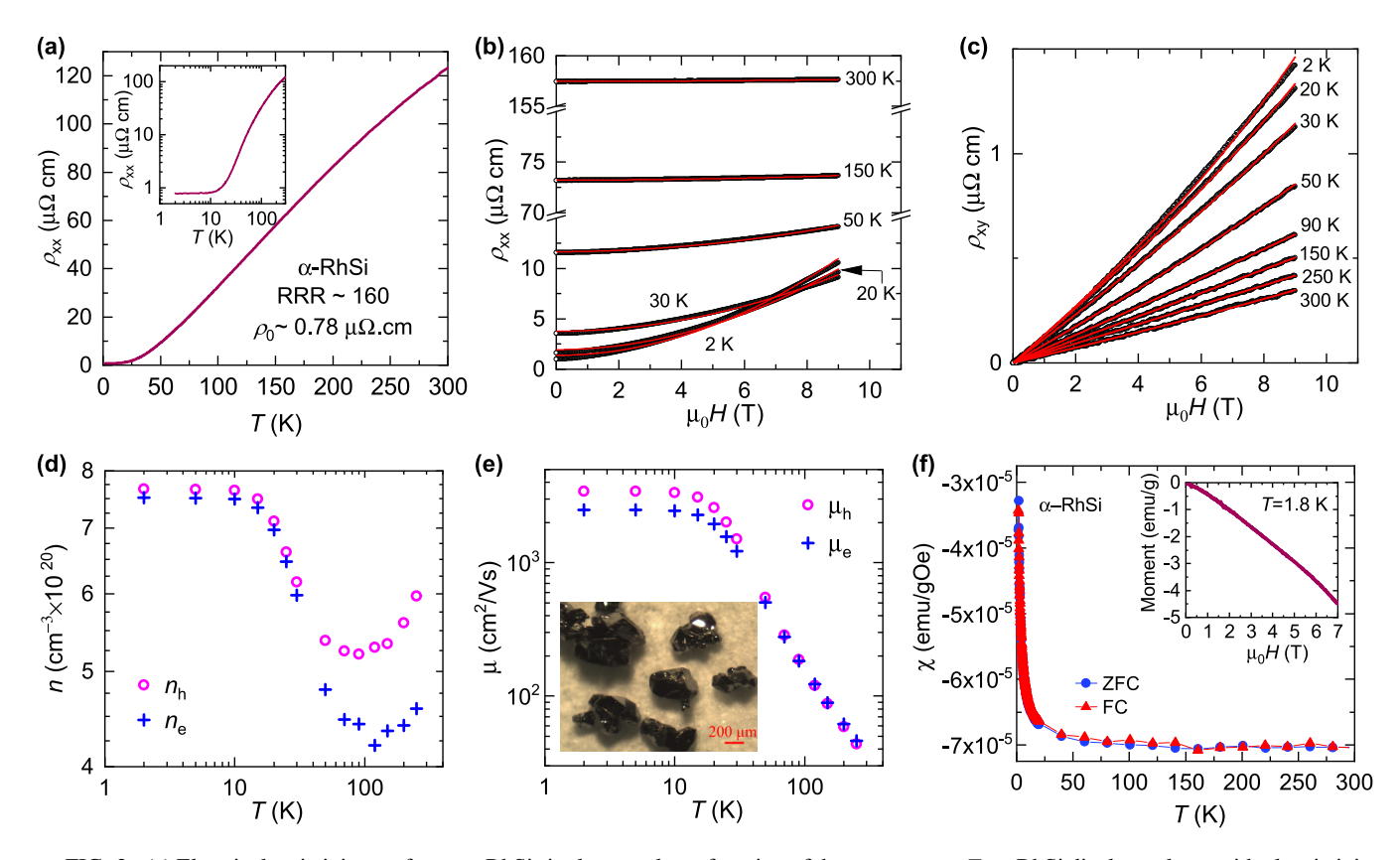


FIG. 2. (a) Electrical resistivity ρ_{xx} for an α -RhSi single crystal as a function of the temperature T. α -RhSi displays a low residual resistivity $\rho_0 = 0.78 \ \mu\Omega$ cm and a residual resistivity ratio (RRR) of 160. Inset: same plot but in a log-log scale. (b) and (c) Longitudinal resistivity ρ_{xx} and Hall resistance ρ_{xy} as a function of the magnetic field and for several temperatures. Red lines are fits of ρ_{xx} and ρ_{xy} to the two-band model [see Eq. (1)]. (d) Charge carrier densities n_e and n_h for electron and holes, respectively, as a function of T. (e) Charge carrier mobilities μ_e and μ_h for electron and holes, respectively, as a function of T. Charge carrier densities and mobilities were extracted from fits to the two-band model. Inset: picture of typical crystals of α -RhSi grown through the use of Te as the flux. (f) Temperature dependence of the magnetic susceptibility measured under fixed magnetic fields after zero-field cooling (ZF) and field cooling (FC). Inset: magnetization as a function of the field at $T = 1.8 \ \text{K}$.

Fig. 2 the magnetization reveals diamagnetic behavior over the entire T range, 1.8 K < T < 300 K, which is consistent with the absence of impurities. Notice that the very small upturn observed in the magnetic susceptibility $\chi(T)$ at low temperatures [see Fig. 2(f)] cannot be fit to a Curie-Weiss term; therefore, it is unlikely to result from magnetic impurities. From measurements of the Hall resistivity and of the magnetoresistivity we estimate the carrier concentrations $n_{e,h}$ and their mobilities $\mu_{e,h}$ through a two-band analysis. $n_{e,h}$ and $\mu_{e,h}$ increase as T is lowered, with this system behaving as a compensated semimetal. More importantly, at T=2 K one extracts high mobilities for holes, i.e., $\mu_h=3727$ cm²/Vs, and electrons, $\mu_e=2491$ cm²/Vs, thus confirming the high quality of our single crystals.

An analysis of the Hall effect and of the magnetoresistivity, through the simplistic two-band model through Eq. (1), yields carrier mobilities well in excess of 1×10^3 cm²/Vs:

$$\rho_{xx} = \frac{1}{e} \frac{(n_h \mu_h + n_e \mu_e) + (n_h \mu_e + n_e \mu_h) \mu_h \mu_e B^2}{(n_h \mu_h + n_e \mu_e)^2 + (n_h - n_e)^2 \mu_h^2 \mu_e^2 B^2},$$

$$\rho_{xy} = \frac{B}{e} \frac{(n_h \mu_h^2 - n_e \mu_e^2) + (n_h - n_e) \mu_h^2 \mu_e^2 B^2}{(n_h \mu_h + n_e \mu_e)^2 + (n_h - n_e)^2 \mu_h^2 \mu_e^2 B^2},$$
(1)

where ρ_{xx} and ρ_{xy} are the longitudinal resistivity and Hall resistivity, respectively; n_e and n_h are the carrier densities for electrons and holes, respectively; and μ_e and μ_h are their corresponding mobilities. The results of simultaneous fitting of ρ_{xx} and ρ_{xy} to Eq. (1) are shown by red lines in Figs. 2(b) and 2(c), respectively. Charge carrier densities and mobilities as a function of temperature are shown in Figs. 2(d) and 2(e), respectively. If, instead, one evaluated the mean transport mobility through the Hall conductivity as done in Ref. [23], one would obtain a value approaching $\bar{\mu}_{tr} = 6667 \text{ cm}^2/\text{Vs}$ (see Fig. 3). Magnetic susceptibility measurements shown in Fig. 2(f) reveal that this system remains diamagnetic over the entire range of temperatures, indicating the absence of a Curie-Weiss component that one would associated with magnetic impurities. Therefore, we conclude that the overall evaluation of our crystals indicates, quite clearly, that the obtained crystals are of high quality or display a very low density of defects and impurities.

IV. BAND STRUCTURE CALCULATIONS AND GROUP SYMMETRY ANALYSIS

In Fig. 4 we show the BZ, its HSPs, and the EBS of α -RhSi. See also Fig. S4 [36] for the EBS depicted over the entire BZ.

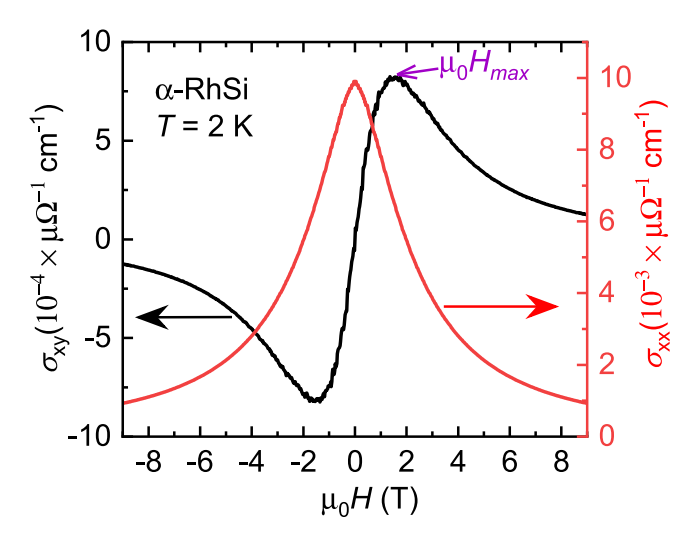


FIG. 3. Electrical conductivity σ_{xx} and Hall conductivity σ_{xy} for an α -RhSi single crystal as a function of the magnetic field $\mu_0 H$. These parameters were obtained by inverting the components ρ_{ij} of the resistivity tensor as a function of $\mu_0 H$. σ_{xy} displays the typical "dispersive-resonance" profile response discussed in detail in Ref. [23], displaying a sharp peak at $\mu_0 H_{\text{max}}$ that reflects the elliptical cyclotron orbits executed by the charge carriers at low fields. From the position of the peak, i.e., 1.5 T, a mean transport mobility $\bar{\mu}_{tr} \simeq (\mu_0 H_{\text{max}})^{-1} \simeq 6667 \text{ cm}^2/\text{Vs}$ is extracted.

It shows that there are fourfold symmetries and the presence of several band crossings. These crossings along several high-symmetry directions can be understood from the symmetry analysis. We will mainly focus on the S HSP because there are band crossings near ε_F . We also show that there should be a NL on the k_y - k_z high-symmetry plane which is caused by these band crossings. The close proximity in energy between these band crossings, which are within the resolution of DFT, requires an independent verification of their existence, hence the group symmetry analysis.

The nonsymmorphic space group *Pnma* (No. 62) [43] has three screw-axis symmetry operations of the general form using Seitz notation, $\{2_{100}|\frac{1}{2}\frac{1}{2}\frac{1}{2}\}$, $\{2_{010}|0\frac{1}{2}0\}$, and $\{2_{001}|\frac{1}{2}0\frac{1}{2}\}$, and the three glide-plane symmetry operations, $\{m_{100}|\frac{1}{2}\frac{1}{2}\frac{1}{2}\}$, $\{m_{010}|0\frac{1}{2}0\}$, and $\{m_{001}|\frac{1}{2}0\frac{1}{2}\}$. There are also TRS and inversion symmetry, which yield Kramers degeneracy. The band representations of the double SG 62 at the various HSPs of the BZ for Wyckoff position 8d:(x,y,z) (the case for α -RhSi) are known [44–47] and can be found in Ref. [48]. The representations of the subgroups of the HSPs R, S, and U, are direct sums of the two four-dimensional representations that include Kramers degeneracy. Due to this additional degeneracy they consist of either a pair of the same irreducible representations (e.g., $\bar{R}_3\bar{R}_3$) or different irreducible representations (IRs; e.g., $\bar{R}_3\bar{R}_4$). At the Γ point there is no such additional degeneracy. These are IRs of the little group corresponding to each high-symmetry k point, and they are subducted along highsymmetry lines (HSLs) that connect them. For example, along the RS high-symmetry manifold, since the symmetry is lower than that of the HSPs that it connects, the IRs $\bar{R}_3\bar{R}_3(4)$ and

 $\bar{R}_4\bar{R}_4(4)$ become reducible to

$$\bar{R}_3\bar{R}_3(4) \to \bar{Q}_3\bar{Q}_3(2) \oplus \bar{Q}_5\bar{Q}_5(2),$$
 (2)

$$\bar{R}_4\bar{R}_4(4) \to \bar{Q}_2\bar{Q}_2(2) \oplus \bar{Q}_4\bar{Q}_4(2).$$
 (3)

Similarly, along the same HSL, the $\bar{S}_3\bar{S}_3(4)$ and $\bar{S}_4\bar{S}_4(4)$ representations are reducible to

$$\bar{S}_3\bar{S}_3(4) \to \bar{Q}_2\bar{Q}_2(2) \oplus \bar{Q}_3\bar{Q}_3(2),$$
 (4)

$$\bar{S}_4\bar{S}_4(4) \to \bar{Q}_4\bar{Q}_4(2) \oplus \bar{Q}_5\bar{Q}_5(2).$$
 (5)

Therefore, these IRs along these HSLs connecting the two HSPs S and R have to be connected as shown schematically in Fig. 5. The compatible band connectivity, an example of which is shown in Fig. 5(a), for any combination of IRs at the two connected HSPs forces the intersection of the bands belonging to different \bar{Q} -type IRs, and this gives rise to a band crossing along these high-symmetry manifolds. By carrying out the same analysis along the other HSLs that start from S, we are concluding that these crossings form a NL.

A somewhat similar band crossing occurs when we consider the breakdown of the IRs along the HSLs which start from HSP S, and they connect the high-symmetry X point (SX line or D manifold), as seen in Fig. 5(b).

The situation along the SY direction is different. Along this symmetry line, $\bar{S}_3\bar{S}_3(4)$ and $\bar{S}_4\bar{S}_4(4)$ at the S point become

$$\bar{S}_3\bar{S}_3(4) \to \bar{C}_5\bar{C}_5(4),$$
 (6)

$$\bar{S}_4\bar{S}_4(4) \to \bar{C}_5\bar{C}_5(4).$$
 (7)

And $\bar{Y}_3\bar{Y}_4(4)$ at the Y point becomes

$$\bar{Y}_3\bar{Y}_4(4) \to \bar{C}_5\bar{C}_5(4).$$
 (8)

Therefore, the SY line becomes a fourfold-degenerate HSL.

Last, we consider the Δ manifold, i.e., the line connecting the Γ and Y HSPs. Along this direction the IRs at the Y point and Γ point reduce as follows:

$$\bar{Y}_3\bar{Y}_4(4) \rightarrow 2\bar{\Delta}_5(2),$$
 (9)

$$\bar{\Gamma}_5(2) \rightarrow \bar{\Delta}_5(2), \quad \bar{\Gamma}_6(2) \rightarrow \bar{\Delta}_5(2).$$
 (10)

Therefore, the $\bar{Y}_3\bar{Y}_4(4)$ representation, which is irreducible at the Y point, reduces to two two-dimensional (2D) representations $\bar{\Delta}_5(2)$ which can directly connect to 2D $\bar{\Gamma}_5(2)$ and $\bar{\Gamma}_6(2)$ IRs at the Γ point without or with any number of band intersections. The latter seems to be the case in the EBS of α -RhSi; namely, the two degenerate bands at the Y point separate along the Y to Γ direction, and then they intersect each other twice along the Δ direction before connecting to the Γ point [see Fig. 4(b)]. The SY line is not the only fourfold high-symmetry manifold. The lines UZ (A manifold), UX (G manifold), UR (P manifold), and RT (E manifold) are all fourfold high-symmetry manifolds.

In the previous discussion we demonstrated that there should be (symmetry-protected) band crossings along HSLs starting from the S HSP. This also became clear from Fig. 4, where we noticed band crossings along the $S\Gamma$, SX, and SR lines. In fact, in Ref. [30], it was shown that a nonsymmorphic symmetry protects a four-band crossing NL in systems with

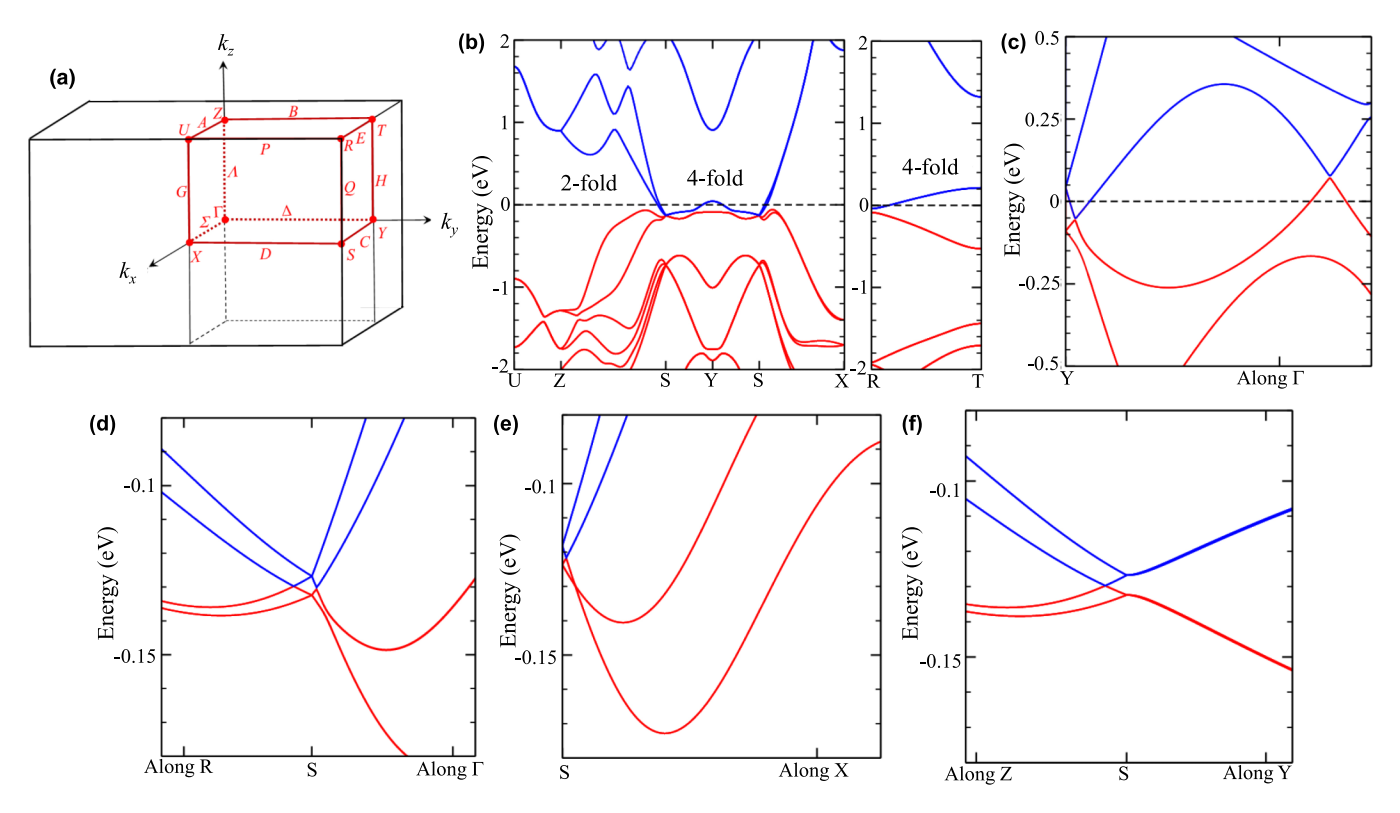


FIG. 4. (a) High-symmetry points on the BZ of orthorhombic α -RhSi. (b) Electronic band structure along various high-symmetry directions where the fourfold high-symmetry BZ boundary lines are indicated. (c)–(f) Band structure along the various high-symmetry directions starting from the S point, i.e., along the $Y\Gamma$, SR and $S\Gamma$, SX, and ZS and SY directions, respectively. Our group theory analysis regarding the connectivity of the S point indicates that there are band crossings along the SR and SX directions.

both inversion symmetry and TRS. This applies directly to our case for the $k_x = \pi$ plane (the plane where the NL lies), which is invariant under the screw-axis operator $\{2_{100}|\frac{1}{2},\frac{1}{2},\frac{1}{2}\}$. This implies that there is a symmetry protected NL around the S point on the k_y - k_z plane. This is illustrated in Fig. 6(a), where on the k_v - k_z plane there are two upside-down Dirac cones intersecting and forming an elliptically shaped NL centered at the S HSP, as shown in Fig. 6(b). To illustrate this, Fig. 6(c) shows a contour plot of the energy of the lower band that intersects a higher energy band as a function of k_v and k_z . In addition, Fig. 6(d) gives a contour plot of the energy difference between these two intersecting Dirac cones. The energy difference between the upper and lower Dirac cones at the S point is only \sim 5 meV. Because the Fermi velocity is $\hbar v_F \sim 1.13$ eV Å along the k_v direction and 0.23 eV Å along the k_z direction, the semimajor axis of the NL is about 0.01 Å^{-1} , and the semiminor axis is about 0.002 Å^{-1} .

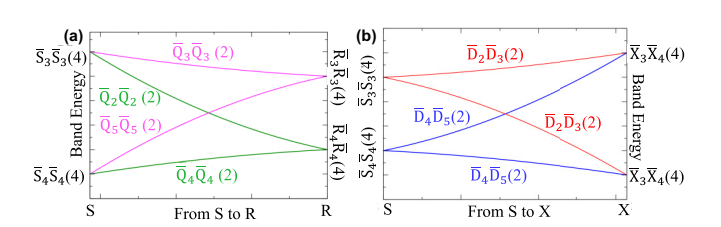


FIG. 5. Band connectivity along the high-symmetry lines (a) SR and (b) SX.

V. DE HAAS-VAN ALPHEN MEASUREMENTS

Finally, we compare the DFT calculations with the angular dependence of the dHvA effect. Figure 7(a) displays the fast Fourier transform (FFT) of the dHvA signal presented in Fig. S3(a) for several values of θ between $\mu_0 H$ and the

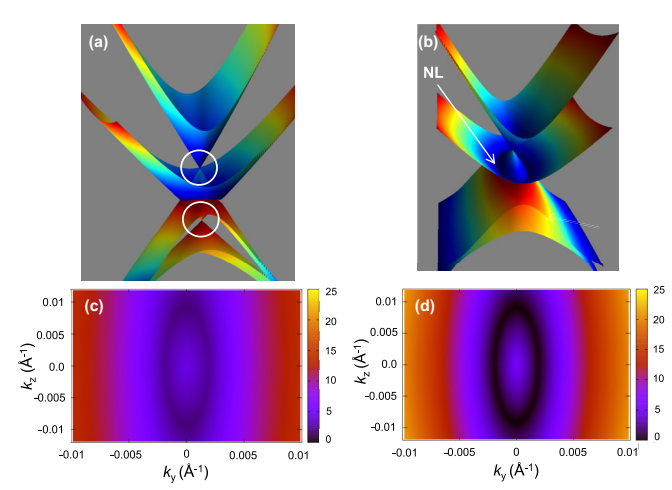


FIG. 6. (a) The band structure at the S point as a function of (k_y, k_z) . (b) Tilted band structure exposing the nodal line on the k_y - k_z plane around the HSP S. Circles and arrows indicate the Dirac nodes and the Dirac nodal line, respectively. (c) Constant-energy contour for the lower band forming the nodal line. (d) Energy difference between the bands forming a nodal line.

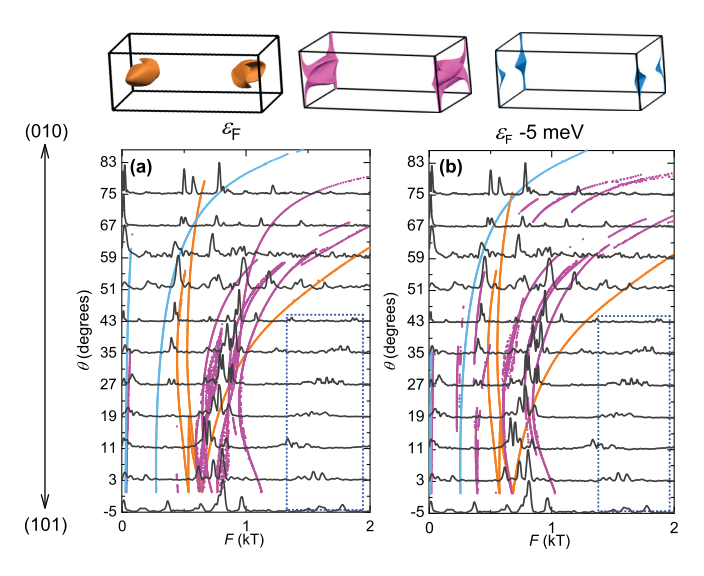


FIG. 7. (a) Fast Fourier transform spectra of the oscillatory component superimposed onto the magnetic torque τ for several angles between $\mu_0 H$ and the (101) direction. These traces are vertically displaced for clarity. The oscillatory data collected at T=350 mK are displayed in Fig. S3(a). Superimposed clear blue, magenta, and orange traces depict the angular dependence of the cyclotron orbits according to the DFT calculations. (b) Same as in (a), but for ε_F displaced by -5 meV. Blue dotted rectangles enclose peaks that correspond to harmonics and hence were not included in our calculations. The top panels display the FS sheets according to the DFT calculations for $\varepsilon_F=0$ meV. Their colors match those of the markers depicting the associated dHvA frequencies.

(101) axis as the field is rotated towards the (010) axis. Each peak, observed at a cyclotron frequency F, is related to a FS cross-sectional area A through the relation $F = \hbar A/2\pi e$. In Figs. 7(a) and 7(b) we superimpose the Fs predicted by the DFT calculations (colored traces) on the experimental FFT spectra. In Fig. 7(a) the theoretical Fs correspond to those resulting from the position of ε_F chosen by our DFT implementation, while in Fig. 7(b) we displace ε_F by -5meV. This small displacement, which is within the systematic error of the DFT calculations, leads to a slightly better agreement between experimental and predicted Fs. Notice that (i) the dominant fundamental peaks observed between 0.5 and 1.5 kT are broadly described by the DFT calculations, thus confirming the validity of our predictions, and (ii) such a small displacement in ε_F does not affect the band structure. FFT peaks observed at higher Fs (enclosed by blue rectangles) correspond to the harmonics of the fundamental ones. Fs on the order of 2 kT predicted by the DFT calculations were not experimentally detected, probably requiring higher fields. In Fig. S3(b) we include the amplitude of the peaks observed in the FFT spectra as a function of T, extracting effective masses ranging from $0.5m_e$ to $1.8m_e$. We emphasize that the existence of the NL is protected by the crystalline symmetry of α -RhSi. The only open issue is its exact location with respect to ε_F . The comparison between dHvA and DFT indicates that the error in the DFT calculations is of the order of 10-20 meV; when we alter the location of ε_F by this amount, the quality of the agreement becomes far worse. This indicates that the error

in the DFT calculations cannot be larger than this amount. We also estimated the effect of electronic correlations for α -RhSi (see Fig. S4) by performing a generalized gradient approximation calculation including an electronic correlation U term [49]. We find that correlations do not affect the existence of the Dirac nodes or Dirac nodal line but yield a somewhat poorer agreement with the experiments (see Fig. S5). Correlations shift the location of the nodal line by only 10–20 meV with respect to this position, thus supporting the robustness of the DFT calculations.

VI. SUMMARY

In summary, we have shown here, through group theory analysis and DFT calculations, that orthorhombic α -RhSi has a complex Dirac dispersion near the Fermi energy. It preserves rotoinversion symmetry, and therefore, instead of being a multifold Weyl fermion system like β -RhSi, it is a unique example of a Dirac semimetallic system, displaying single, as well as double, Dirac nodes in close proximity to the ε_F (within 100 and 150 meV from ε_F). The double Dirac dispersions, emerging from the S point with only 5-meV distance between the corresponding pair of Dirac points, intersect, forming a nodal line in the k_v - k_z plane protected by the nonsymmorphic symmetry of α -RhSi. This double Dirac structure and the associated Dirac nodal line are similar to what was proposed for the correlated iridate CaIrO₃ [34,50]. However, in contrast to SrIrO₃ or CaIrO₃, in orthorhombic α -RhSi all bands crossing ε_F emerge directly from the Dirac nodes. Among Dirac systems only Na₃Bi seems to display a single Diraclike crossing near ε_F [35]. As for Dirac nodal line systems, only IrO₂ displays symmetry protected Dirac nodal lines in proximity to ε_F but coexisting with topologically trivial bands [51]. As discussed in Ref. [3], it is of paramount importance to identify compounds like α -RhSi that display band crossings very close to ε_F leading, for example, to Dirac and Weyl nodes but with no other bands crossing it. Measurements of the de Haas-van Alphen effect in high-quality flux-grown single crystals reveal a Fermi surface whose topography is in broad good agreement with the DFT predictions, thus validating the band structure calculations. The anomalous behavior of the magnetic torque observed for certain field orientations points to the possibility of transitions between distinct topological regimes as the Zeeman effect displaces the spin-orbit split bands and lifts the Kramers degeneracy of the dual Dirac dispersion.

ACKNOWLEDGMENTS

L.B. is supported by the US Department of Energy, Basic Energy Sciences program through Award No. DE-SC0002613. S.M. acknowledges support from the FSU Provost Postdoctoral Fellowship Program. J.Y.C. acknowledges support from the US National Science Foundation (NSF) Grant No. DMR-1700030. The National High Magnetic Field Laboratory acknowledges support from US NSF Cooperative Agreement Grant No. DMR-1644779 and the state of Florida. The data in this paper can be assessed by requesting them from the corresponding authors.

- [1] P. B. Pal, Am. J. Phys. 79, 485 (2011).
- [2] N. P. Armitage, E. J. Mele, and A. Vishwanath, Rev. Mod. Phys. 90, 015001 (2018).
- [3] A. A. Burkov, Nat. Mater. 15, 1145 (2016).
- [4] A. Burkov, Annu. Rev. Condens. Matter Phys. 9, 359 (2018).
- [5] J. Hu, S.-Y. Xu, N. Ni, and Z. Mao, Annu. Rev. Mater. Phys. Res. 49, 207 (2019).
- [6] H. Weng, X. Dai, and Z. Fang, J. Phys.: Condens. Matter 28, 303001 (2016).
- [7] B. J. Wieder, Y. Kim, A. M. Rappe, and C. L. Kane, Phys. Rev. Lett. 116, 186402 (2016).
- [8] B. Bradlyn, J. Cano, Z. Wang, M. G. Vergniory, C. Felser, R. J. Cava, and B. A. Bernevig, Science 353, aaf5037 (2016).
- [9] P. Tang, Q. Zhou, and S.-C. Zhang, Phys. Rev. Lett. 119, 206402 (2017).
- [10] D. A. Pshenay-Severin, Y. V. Ivanov, A. A. Burkov, and A. T. Burkov, J. Phys.: Condens. Matter 30, 135501 (2018).
- [11] H. Weng, C. Fang, Z. Fang, and X. Dai, Phys. Rev. B 94, 165201 (2016).
- [12] G. Chang, S.-Y. Xu, B. J. Wieder, D. S. Sanchez, S.-M. Huang, I. Belopolski, T.-R. Chang, S. Zhang, A. Bansil, H. Lin, and M. Z. Hasan, Phys. Rev. Lett. 119, 206401 (2017).
- [13] Z. Rao, H. Li, T. Zhang, S. Tian, C. Li, B. Fu, C. Tang, L. Wang, Z. Li, W. Fan, J. Li, Y. Huang, Z. Liu, Y. Long, C. Fang, H. Weng, Y. Shi, H. Lei, Y. Sun, T. Qian, and H. Ding, Nature (London) 567, 496 (2019).
- [14] D. Takane, Z. Wang, S. Souma, K. Nakayama, T. Nakamura, H. Oinuma, Y. Nakata, H. Iwasawa, C. Cacho, T. Kim, K. Horiba, H. Kumigashira, T. Takahashi, Y. Ando, and T. Sato, Phys. Rev. Lett. 122, 076402 (2019).
- [15] D. S. Sanchez, I. Belopolski, T. A. Cochran, X. Xu, J.-X. Yin, G. Chang, W. Xie, K. Manna, V. Süß, C.-Y.Huang, N. Alidoust, D. Multer, S. S. Zhang, N. Shumiya, X. Wang, G.-Q. Wang, T.-R. Chang, C. Felser, S.-Y. Xu, S. Jia, H. Lin, and M. Z. Hasan, Nature (London) 567, 500 (2019).
- [16] N. B. M. Schröter, D. Pei, M. G. Vergniory, Y. Sun, K. Manna, F. de Juan, J. A. Krieger, V. Süss, M. Schmidt, P. Dudin, B. Bradlyn, T. K. Kim, T. Schmitt, C. Cacho, C. Felser, V. N. Strocov, and Y. Chen, Nat. Phys. 15, 759 (2019).
- [17] H. Li, S. Xu, Z.-C. Rao, L.-Q. Zhou, Z.-J. Wang, S.-M. Zhou, S.-J. Tian, S.-Y. Gao, J.-J. Li, Y.-B. Huang, H.-C. Lei, H.-M. Weng, Y.-J. Sun, T.-L. Xia, T. Qian, and H. Ding, Nat. Commun. 10, 5505 (2019).
- [18] N. B. M. Schröter, S. Stolz, K. Manna, F. de Juan, M. G. Vergniory, J. A. Krieger, D. Pei, P. Dudin, T. K. Kim, C. Cacho, B. Bradlyn, H. Borrmann, M. Schmidt, R. Widmer, V. Strokov, and C. Felser, Science 369, 179 (2020).
- [19] T. Morimoto and N. Nagaosa, Phys. Rev. Lett. 117, 146603 (2016).
- [20] F. de Juan, A. G. Grushin, T. Morimoto, and J. E. Moore, Nat. Commun. 8, 15995 (2017).
- [21] F. Flicker, F. de Juan, B. Bradlyn, T. Morimoto, M. G. Vergniory, and A. G. Grushin, Phys. Rev. B 98, 155145 (2018).
- [22] Z. K. Liu, J. Jiang, B. Zhou, Z. J. Wang, Y. Zhang, H. M. Weng, D. Prabhakaran, S.-K. Mo, H. Peng, P. Dudin, T. Kim, M. Hoesch, Z. Fang, X. Dai, Z. X. Shen, D. L. Feng, Z. Hussain, and Y. L. Chen, Nat. Mater. 13, 677 (2014).
- [23] T. Liang, Q. Gibson, M. N. Ali, M. Liu, R. J. Cava, and N. P. Ong, Nat. Mater. 14, 280 (2015).

- [24] Z. K. Liu, B. Zhou, Y. Zhang, Z. J. Wang, H. M. Weng, D. Prabhakaran, S.-K. Mo, Z. X. Shen, Z. Fang, X. Dai, Z. Hussain, and Y. L. Chen, Science 343, 864 (2014).
- [25] J. Xiong, S. K. Kushwaha, T. Liang, J. W. Krizan, M. Hirschberger, W. Wang, R. J. Cava, and N. P. Ong, Science 350, 413 (2015).
- [26] A. C. Potter, I. Kimchi, and A. Vishwanath, Nat. Commun. 5, 5161 (2014).
- [27] P. J. W. Moll, N. L. Nair, T. Helm, A. C. Potter, I. Kimchi, A. Vishwanath, and J. G. Analytis, Nature (London) 535, 266 (2016).
- [28] C. Zhang, Y. Zhang, X. Yuan, S. Lu, J. Zhang, A. Narayan, Y. Liu, H. Zhang, Z. Ni, R. Liu, E. S. Choi, A. Suslov, S. Sanvito, L. Pi, H.-Z. Lu, A. C. Potter, and F. Xiu, Nature (London) 565, 331 (2019).
- [29] A. A. Burkov, M. D. Hook, and L. Balents, Phys. Rev. B 84, 235126 (2011).
- [30] C. Fang, Y. Chen, H.-Y. Kee, and L. Fu, Phys. Rev. B 92, 081201(R) (2015).
- [31] C. Fang, H. Weng, X. Dai, and Z. Fang, Chin. Phys. B 25, 117106 (2016).
- [32] Y.-C. Chiu, K.-W. Chen, R. Schönemann, V. L. Quito, S. Sur, Q. Zhou, D. Graf, E. Kampert, T. Förster, K. Yang, G. T. McCandless, J. Y. Chan, R. E. Baumbach, M. D. Johannes, and L. Balicas, Phys. Rev. B 100, 125112 (2019).
- [33] L. M. Schoop, M. N. Ali, C. Straßer, A. Topp, A. Varykhalov, D. Marchenko, V. Duppel, S. S. P. Parkin, B. V. Lotsch, and C. R. Ast, Nat. Commun. 7, 11696 (2016).
- [34] J. Fujioka, R. Yamada, M. Kawamura, S. Sakai, M. Hirayama, R. Arita, T. Okawa, D. Hashizume, M. Hoshino, and Y. Tokura, Nat. Commun. 10, 362 (2019).
- [35] S.-Y. Xu, C. Liu, S. K. Kushwaha, R. Sankar, J. W. Krizan, I. Belopolski, M. Neupane, G. Bian, N. Alidoust, T.-R. Chang, H.-T. Jeng, C.-Y. Huang, W.-F. Tsai, H. Lin, P. P. Shibayev, F.-C. Chou, R. J. Cava, and M. Z. Hasan, Science 347, 294 (2015).
- [36] See Supplemental Material at http://link.aps.org/supplemental/ 10.1103/PhysRevB.102.115131 for experimental details, x-ray characterization of the flux-grown RhSi single crystals, resistivity, Hall effect, magnetic susceptibility, evaluation of carrier densities and mobilities, angular evolution of the torque components, raw oscillatory signals, their Fourier transforms and extraction of effective masses, details concerning density functional theory, and generalized gradient approximation calculations.
- [37] J. P. Perdew, K. Burke, and M. Ernzerhof, Phys. Rev. Lett. 78, 1396 (1997).
- [38] P. Giannozzi, S. Baroni, N. Bonini, M. Calandra, R. Car, C. Cavazzoni, D. Ceresoli, *et al.*, J. Condens. Matter Phys. 21, 395502 (2009).
- [39] D. R. Hamann, Phys. Rev. B 88, 085117 (2013).
- [40] A. A. Mostofi, J. R. Yates, G. Pizzi, Y.-S. Lee, I. Souza, D. Vanderbilt, and N. Marzari, Comput. Phys. Commun. 185, 2309 (2014).
- [41] K. Schwarz, P. Blaha, and G. Madsen, Comput. Phys. Commun. 147, 71 (2002).
- [42] P. Rourke and S. Julian, Comput. Phys. Commun. 183, 324 (2012).
- [43] C. J. Bradley and A. Cracknell, *The Mathematical Theory of Symmetry in Solids* (Oxford, 1972).

- [44] L. Elcoro, B. Bradlyn, Z. Wang, M. G. Vergniory, J. Cano, C. Felser, B. A. Bernevig, D. Orobengoa, G. de la Flor, and M. I. Aroyo, J. Appl. Crystallogr. 50, 1457 (2017).
- [45] B. Bradlyn, L. Elcoro, J. Cano, M. G. Vergniory, Z. Wang, C. Felser, M. I. Aroyo, and B. A. Bernevig, Nature (London) 547, 298 (2017).
- [46] M. G. Vergniory, L. Elcoro, Z. Wang, J. Cano, C. Felser, M. I. Aroyo, B. A. Bernevig, and B. Bradlyn, Phys. Rev. E 96, 023310 (2017).
- [47] J. Kruthoff, J. de Boer, J. van Wezel, C. L. Kane, and R.-J. Slager, Phys. Rev. X 7, 041069 (2017).
- [48] M. I. Aroyo, J. M. Perez-Mato, D. Orobengoa, E. Tasci, G. de la Flor, and A. Kirov, Bulg. Chem. Commun. **43**, 183 (2011).
- [49] A. I. Liechtenstein, V. I. Anisimov, and J. Zaanen, Phys. Rev. B 52, R5467 (1995).
- [50] J.-M. Carter, V. V. Shankar, M. A. Zeb, and H.-Y. Kee, Phys. Rev. B 85, 115105 (2012).
- [51] J. N. Nelson, J. P. Ruf, Y. Lee, C. Zeledon, J. K. Kawasaki, S. Moser, C. Jozwiak, E. Rotenberg, A. Bostwick, D. G. Schlom, K. M. Shen, and L. Moreschini, Phys. Rev. Mater. 3, 064205 (2019).